Monthly Notices
of the
ROYAL ASTRONOMICAL SOCIETY

MNRAS **497,** 2529–2539 (2020)
Advance Access publication 2020 July 24

doi:10.1093/mnras/staa2133

Noise from undetected sources in Dark Energy Survey images

K. Eckert,[1] G. M. Bernstein ,[1]★ A. Amara,[2] A. Amon,[3] A. Choi,[4] S. Everett,[5] D. Gruen,[3,6,7] R. A. Gruendl,[8,9] E. M. Huff,[10] N. Kuropatkin,[11] A. Roodman,[3,7] E. Sheldon,[12] B. Yanny,[11] Y. Zhang,[11] T. M. C. Abbott,[13] M. Aguena,[14,15] S. Avila,[16] K. Bechtol,[17,18] D. Brooks,[19] D. L. Burke,[3,7] A. Carnero Rosell,[20,21] M. Carrasco Kind,[8,9] J. Carretero,[22] M. Costanzi,[23,24] L. N. da Costa,[15,25] J. De Vicente,[26] S. Desai,[27] H. T. Diehl,[11] J. P. Dietrich,[28] T. F. Eifler,[29,10] A. E. Evrard,[30,31] B. Flaugher,[11] J. Frieman,[11,32] J. García-Bellido,[16] E. Gaztanaga,[33,34] J. Gschwend,[15,25] G. Gutierrez,[11] W. G. Hartley,[35,19,2] D. L. Hollowood,[5] K. Honscheid,[4,36] D. J. James,[37] R. Kron,[11,32] K. Kuehn,[38,39] M. A. G. Maia,[15,25] J. L. Marshall,[40] P. Melchior,[41] F. Menanteau,[8,9] R. Miquel,[22,42] R. L. C. Ogando,[15,25] A. Palmese,[11,32] F. Paz-Chinchón,[9,43] A. A. Plazas,[41] A. K. Romer,[44] E. Sanchez,[26] V. Scarpine,[11] S. Serrano,[33,34] I. Sevilla-Noarbe,[26] M. Smith,[45] M. Soares-Santos,[46] E. Suchyta,[47] M. E. C. Swanson,[9] G. Tarle,[31] D. Thomas,[48] T. N. Varga,[49,50] A. R. Walker,[13] W. Wester,[11] R.D. Wilkinson[44] and J. Zuntz[51] (The DES Collaboration)

Affiliations are listed at the end of the paper

Accepted 2020 July 7. Received 2020 June 12; in original form 2020 April 22

ABSTRACT

For ground-based optical imaging with current CCD technology, the Poisson fluctuations in source and sky background photon arrivals dominate the noise budget and are readily estimated. Another component of noise, however, is the signal from the undetected population of stars and galaxies. Using injection of artifical galaxies into images, we demonstrate that the measured variance of galaxy moments (used for weak gravitational lensing measurements) in Dark Energy Survey (DES) images is significantly in excess of the Poisson predictions, by up to 30 per cent, and that the background sky levels are overestimated by current software. By cross-correlating distinct images of 'empty' sky regions, we establish that there is a significant image noise contribution from undetected static sources (US), which, on average, are mildly resolved at DES resolution. Treating these US as a stationary noise source, we compute a correction to the moment covariance matrix expected from Poisson noise. The corrected covariance matrix matches the moment variances measured on the injected DES images to within 5 per cent. Thus, we have an empirical method to statistically account for US in weak lensing measurements, rather than requiring extremely deep sky simulations. We also find that local sky determinations can remove most of the bias in flux measurements, at a small penalty in additional, but quantifiable, noise.

Key words: gravitational lensing: weak – techniques: image processing – diffuse radiation.

1 INTRODUCTION

Optical images from modern astronomical surveys are subject to noise coming both from the detector and from shot noise of arriving source and background photons. By taking calibration data, we can accurately measure the detector read noise, and calculate the detector gain to yield an accurate Poisson noise estimate. Nuisance signals such as cosmic rays or satellite trails can be identified with streak finders and excised from the data. Together, these standard techniques yield an estimate of the total noise in the image. Many astrophysical investigations require very accurate estimation of the image noise and background levels in order to obtain unbiased inferences. We will focus on weak graviational lensing (WL) measurements of the shapes of galaxies, but other astrophysical investigations, e.g. searches for flux variability, depend heavily on accurate knowledge of the *uncertainties* in source measurements.

There is, however, an additional source of noise in background-limited images, which is typically ignored: the contribution from undetected background (or foreground) sources (US), which will add noise above the Poisson expectation for the mean background flux. Some studies have examined the effect of US on specific methods of WL shear measurement. For example, Hoekstra, Viola & Herbonnet (2017) find that calibration simulations must include undetected background galaxies with $m_{F606W} \sim 29$ to ensure calibrated multiplicative biases $<1 \times 10^{-4}$ for the 'KSB' estimator of WL shear (Kaiser, Squires & Broadhurst 1995). For the IM3SHAPE estimator (Zuntz et al. 2013), Samuroff et al. (2018) find that the contribution to the bias from undetected background galaxies is well below statistical uncertainties for the year 1 analysis of the Dark Energy Survey (DES; Drlica-Wagner et al. 2018). Most recently, Euclid Collaboration (2019) show that undetected background galaxies with

★ E-mail: garyb@physics.upenn.edu

magnitude down to ∼28 must be included to calibrate the shear measurement bias for three methods: KSB, Source Extractor+PSFEx (Bertin 2011), and MomentsML (Tewes et al. 2019).

Here we propose a different way to characterize the contribution of US in the context of the Bayesian Fourier Domain (BFD) shear measurement method (Bernstein & Armstrong 2014; Bernstein et al. 2016). The BFD method is a rigorous Bayesian shape measurement algorithm that is unbiased and does not require simulations for calibrations. Unlike other shear measurement algorithms, BFD does not produce point estimates of shape, but instead estimates the shear, given each source's image data by comparing to an unsheared prior population of noiseless 'template' galaxies (typically drawn from the deep survey within a typical WL photometric survey). BFD compresses the information on each galaxy to its image moments of order 0, 1, and 2. These moments are measured in Fourier domain, after correction for the point spread function (PSF), so that the mean result is independent of image seeing. These BFD observables are chosen to be linear in the pixel values, enabling accurate propagation of the image noise into a known multivariate Gaussian distribution for the vector of BFD moments.

In this work, we examine the noise distributions for BFD moment measurements in real DES data by adding artificial galaxies to the real images, then measuring their moments. The DES image-injection process is known as 'Balrog' (Suchyta et al. 2016; Everett et al., in preparation). We first show that there is unaccounted-for noise by looking at the BFD moment distribution of injected galaxies. We then measure the statistics of US in DES images by cross-correlating distinct exposures of 'empty' sky, i.e. regions where no sources are above the detection threshold. In this cross-correlation between exposures, all temporally stochastic noise sources, namely read noise and shot noise, will average to zero. This technique is similar in spirit to the surface brightness fluctuation distance measurement technique (Tonry & Schneider 1988) and to estimations of the contribution of high-redshift sources to the luminosity function (Kashlinsky et al. 2005, 2012; Calvi et al. 2013). Examination of the injected moments also reveals a bias in the background (sky) level estimation in the current DES pipeline.

Secondly, we show that the US noise can be treated as a quasi-stationary noise source that simply adds to the covariance matrix of BFD moments computed from shot noise. The distribution of moment noise measured from injection of artificial images into the DES data is shown to be in good agreement with the multivariate Gaussian distribution described by this augmented covariance matrix. This treatment of the US noise is ideal because (1) it uses the data themselves to measure the contribution rather than relying on simulations of unknown fidelity and (2) it includes the US contribution as a source of noise organically within the Bayesian calculation, rather than trying to calibrate a bias term after the fact.

In Section 2, we present a summary of the DES data, the Balrog image-injection program, and the BFD shear measurement algorithm. We then describe our characterization of image noise using the BFD moments. In Section 3, we first show that there is excess noise and bias in the BFD moment distribution using injection tests. We also examine the behaviour of the sky-level bias, and find it substantially reduced by a per-object local sky estimation. We then cross-correlate images of empty sky, revealing the buried US signal. Using these same empty regions, we define a cross-covariance matrix for BFD moments that can be added to the shot noise matrix, improving our estimate of the variance in BFD moment distributions. In Section 4, we provide a short description of the properties of the US population and discuss some of the assumptions made in this work. In Section 5, we summarize this work and describe the path forward for the BFD shear measurement algorithm.

2 DATA AND METHODS

In this section, we describe the data and methods used to characterize the noise properties of DES images.

2.1 DES Y3 data

DES is a 6-yr program to image ∼5000 deg^2 of the sky using the Dark Energy Camera installed on the Blanco telescope. The survey is conducted in the *g*, *r*, *i*, *z*, and *Y* bands aiming for a nominal depth of ∼24th magnitude. For this work, we use the data obtained through year 3 of the program (Y3 data). These data cover the entire DES footprint with typically ∼5 exposures (of a final total of ∼10 exposures) per filter per region of the sky. The rough 10σ point source limiting magnitudes are 24.2, 24.0, 23.5, and 22.8 in the *g*, *r*, *i*, and *z* bands, respectively. We exclude the *Y* band from this analysis since it is much shallower than the *griz* data.

DES images are processed in several steps as described in Morganson et al. (2018). First, the images undergo several pre-processing steps including cross-talk, overscan, bias, and flat-field corrections. Next, the pipeline applies astrometric solutions, performs sky background subtraction, identifies and masks cosmic rays and satellite streaks, and finally detects objects from a *gri* coadd image via Source Extractor (Bertin & Arnouts 1996). The data are output into a Multiepoch Data Structure (MEDS; Jarvis et al. 2016) consisting of postage stamps (typically 32 × 32 pixels, or 8.5 arcsec^2) and basic data for each detected object. Photometric measurements are produced by multiepoch, multiobject fitting (MOF; Drlica-Wagner et al. 2018).

Of most importance to this work is the sky background subtraction routine performed on the single-epoch images, which is described in Morganson et al. (2018). For DES Y3 data, a sky background 'template' set is derived as the first four principal components of a set of ≈1000 images taken in a given filter and observing season. For an individual exposure, a weighted sum of these four templates is constructed to best match the observed background (after reducing the image and templates to the medians of 128 × 128 pixel^2 regions). This weighted sum is then subtracted from the image, and the inverse number of detected sky photons in the background model (plus a contribution from read noise) is saved as the weight map (inverse variance) of the image. This 'PCA' background is hundreds to thousands of photoelectrons per pixel, depending on the filter, lunar phase, etc.

A subsequent background estimation algorithm is applied to each exposure during the cataloging process. This step is performed by the SExtractor sky-estimation algorithm in its `GLOBAL` mode, whereby medians of regions of size `BACK_SIZE` = 256-pixel^2 regions are arrayed, smoothed with a 3 × 3 median filter, and interpolated back to single-pixel resolution [see Morganson et al. (2018) for full details on SExtractor parameter settings]. The SExtractor sky estimation is needed to account for scattered light from the brightest stars, Galactic dust, and other artefacts that are specific to individual pointings and not captured by the PCA. These corrections are typically $O(10)$ photoelectrons per pixel or less, i.e. a small perturbation to the PCA sky. For each exposure/object combination, a postage stamp image is saved to the MEDS file, which already has the PCA sky and the SExtractor sky estimate subtracted. The standard procedure for analysing images is to assume that the MEDS stamp has zero background. We note that the sky background process described here is more complex than the process for DES Y1 images, which relied only on Source Extractor local estimates (Drlica-Wagner et al. 2018).

2.2 Balrog

The Balrog pipeline aims to assess detection efficiency, selection biases, and other biases by injecting fake galaxies with known input parameters into real DES images and running the object detection and photometry as for the real data (Suchyta et al. 2016). The current Balrog analysis for DES Y3 injects parametric galaxy models, with the population of injection galaxies drawn from MOF fits to galaxies found in the DES deep fields, as detailed in Everett et al. (in preparation) and Choi et al. (in preparation). These deep-field images are produced by summing the many exposures taken by DES in each of the 10 supernova-search fields and in the COSMOS field. The deep fields are ∼1 mag deeper than the Y3 DES coadds. The injections are done on the single-epoch images, which are then run through the processing steps for coaddition, object detection, MEDS making, and photometry outputs such as MOF. DES coadd creation, and the Balrog processing, are executed in units of 0.5 deg^2 patches of sky known as 'tiles'. In this work, we make use of 48 tiles for which the full Balrog injection and reanalysis have been completed. We label these as the 'Balrog-injection' tiles. An average of ∼3000 Balrog injections are detected in each tile, though only a subset of them will pass the isolation and S/N cuts that we impose for measurements in this paper.

We also run a variant of the Balrog pipeline to produce MEDS files containing nominally empty patches of sky. This is done by running the Balrog pipeline but skipping the step where the galaxies are actually added to the images. Postage stamps of these 'ghost' Balrog injections thus do not contain any central injected galaxy, but may include real galaxies that were located nearby. We discard any ghost stamps that are located close enough to a detected real object that its detected isophotes impinge on the stamp, leaving us with a MEDS file of apparently source-free but otherwise random regions of sky. We label these DES tiles as 'Balrog-variant' tiles, of which we have 39 for analysis in this work.

2.3 BFD

The BFD shear measurement algorithm is a rigorous Bayesian computation of shear, given the data for an ensemble of galaxies. It does not require simulations for calibrating biases. The method compresses pixel-level data to seven moments computed in Fourier space. A template population of galaxies measured in low-noise imaging serves as prior knowledge on the galaxy population in this moment space. The heart of BFD is to integrate each target galaxy's measured likelihood of moments against a prior embodied by a sheared version of the template population, to produce a posterior probability for the shear, given the observed moments. The individual galaxies' shear posteriors are multiplied to obtain the probability of shear, given the full galaxy sample.

The seven BFD moments are defined as

$$\boldsymbol{M} \equiv \begin{pmatrix} M_F \\ M_X \\ M_Y \\ M_R \\ M_1 \\ M_2 \\ M_C \end{pmatrix} = \int \mathrm{d}^2k \frac{\tilde{I}(k)}{\tilde{T}(k)} W(k^2) \boldsymbol{F}; \boldsymbol{F} = \begin{pmatrix} 1 \\ k_x \\ k_y \\ k_x^2 + k_y^2 \\ k_x^2 - k_y^2 \\ 2k_x k_y \\ \left(k_x^2 + k_y^2\right)^2 \end{pmatrix}. \quad (1)$$

where $\tilde{I}(k)$ is the Fourier transform of the galaxy postage stamp, $\tilde{T}(k)$ is the Fourier transform of the PSF, and $W(k^2)$ is a weight function designed to prevent the integral from going to infinity where the PSF goes to zero. M_F is the zeroth-order flux moment; M_X and M_Y are the first-order centroid moments; M_R, M_1, and M_2 are the second-order shape/size moments; and M_C is a fourth-order moment approximating concentration. In practice, we use fast Fourier transforms (FFTs) to obtain the Fourier transform of the postage stamp and the integral becomes a sum over k-space. When measuring the moments for a galaxy, we centroid on the galaxy by zeroing the first order M_X and M_Y moments and then measure the five other moments. In the standard processing, the level of sky in the MEDS postage stamp is assumed to be zero, i.e. the SExtractor sky estimate is correct, which affects only the $k = 0$ element of $\tilde{I}$. We will investigate an alternative sky subtraction in Section 3.1.

In this work, we use the '$k\sigma$' weight function defined in Bernstein et al. (2016) and given in equation (2). In practice, any weight function could be employed, given two conditions: (1) The weight function goes to zero before the PSF to keep the moment measurement finite, and (2) the weight function has continuous first and second derivatives to enable measurement of the derivatives under shear for the template galaxies:

$$W(k^2) = \begin{cases} \left(1 - \frac{k^2\sigma^2}{2N}\right)^N & k < \frac{\sqrt{2N}}{\sigma} \\ 0 & k \geq \frac{\sqrt{2N}}{\sigma} \end{cases}. \quad (2)$$

One major assumption of BFD is that the pixel noise in the image is stationary and the probability distribution of the observed moments can be described as a multidimensional Gaussian about the true moments, with covariance matrix elements for the ith and jth moment, which can be computed from the power spectrum of the noise $P_n(k)$:

$$\mathbf{Cov}_M[i, j] = \int \mathrm{d}^2k P_n(k) \left|\frac{W(k^2)}{\tilde{T}(k)}\right|^2 F_i(k) F_j(k). \quad (3)$$

In the case of sky background and detector read noise, which should both have white-noise spectra, these conditions are upheld. In the presence of significant shot noise from the source itself, the assumption is not valid. For weak lensing, the majority of our signal comes from faint galaxies where the source shot noise should be insignificant.

In Bernstein et al. (2016), it was shown that the BFD method could produce a nearly unbiased result on postage stamp simulations. There was a remaining multiplicative bias of ∼0.002, which was not explained. In the Appendix, we present updated validation simulations, showing that the method is unbiased within next-generation survey goals of $|m| < 0.002$. Briefly, we find that zero-padding the images (i.e. augmenting the image with regions of zero flux before conducting the Fourier transform) produces more accurate measurements of the moments and their derivatives under shear, since zero-padding produces finer sampling (and better interpolation) of the Fourier space image.

2.4 Noise tests

The accuracy of BFD shear estimates has been assessed in image simulations in which the noise is constructed to be stationary and Gaussian. These conditions must be verified in real data. The Balrog simulations are perfect for validating these assumptions for BFD in a real data setting, since we can measure the true moments M_T of injected galaxies and compare with their measured moments M_D relative to the noise distribution expected from the known levels of sky background noise and detector read noise.

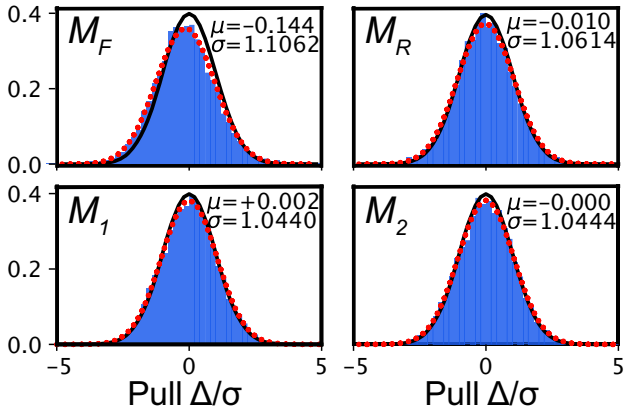

Figure 1. Histograms of χ_M for four BFD moments, namely (a) M_F , (b) M_R , (c) M_1, and (d) M_2, for one DES Balrog-injection tile in the i band. The μ and σ values for a Gaussian fit to each moment's data are given and shown by the red dotted curve. The black curve shows the unit Gaussian. The flux moment shows the largest deviation from a unit Gaussian. In each histogram, there are ∼7000 data points; thus, the formal 1σ uncertainties on the mean and standard deviation are ∼0.01 and ∼0.008, respectively.

We conduct two tests in this vein. First, we define the quantity χ_M for a particular moment M with expected standard deviation σ_M, often called the 'pull':

$$\chi_M = \frac{M_D - M_T}{\sigma_M}. \tag{4}$$

If our noise estimate σ_M is correct, then the distribution of χ_M should follow that of a unit normal ($\mu = 0.0$, $\sigma = 1.0$). If we see that the σ of our distributions is larger than 1.0, then there is some extra noise component unaccounted for in our data. If it is smaller than 1.0, then we might suspect that the noise level has been overestimated.

Alternatively, we can examine the distribution of χ^2_M, which should follow a χ^2 distribution with 1 degree of freedom (also yielding $\langle\chi^2_M\rangle = 1$). This alternative test can be generalized to N galaxy moments:

$$\chi^2_M = (\boldsymbol{M}_D - \boldsymbol{M}_T)^T \, \mathbf{Cov}_M{}^{-1} \, (\boldsymbol{M}_D - \boldsymbol{M}_T)\,, \tag{5}$$

where $\boldsymbol{M}_D$ and $\boldsymbol{M}_T$ are vectors containing N BFD moments. The generalized χ^2_M distribution should follow a χ^2 distribution with N degrees of freedom and yield $\langle\chi^2_M\rangle = N$.

3 NOISE PROPERTIES OF DES IMAGES

In the following sections, we examine the noise properties of DES images. We start by performing the noise tests described in Section 2.4 on the Balrog tiles, finding excess noise. We then look at the cross-correlation of blank sky regions to examine whether this excess noise is due to US. Finally, we characterize the US noise contribution and suggest a way to mitigate its effect for the BFD method.

3.1 Balrog tests

To characterize the noise in DES images, we perform the tests described in Section 2.4 for 48 Balrog-injection tiles randomly selected from the full DES footprint. In Figs 1 and 2, we show the results of the two noise tests for one DES Balrog-injection tile (DES0332−3206) in the i band. For these tests, we select sources with S/N in M_F between 3–20 and having no detected neighbors closer than 5 arcsec. These requirements leave us with ∼7000 separate images of the injected galaxies, which counts images of the same galaxy injected on different exposures as distinct. Across all 48 Balrog-injection tiles, there are ∼300 000 injections meeting those requirements. In Fig. 1, we show the histograms of χ_M for four BFD moments, the zeroth-order flux moment (M_F), and the three second-order shape moments (M_R, M_1, M_2) along with the Gaussian fit to the data (red dotted line) and the unit normal distribution (black). In Fig. 2, we show the cumulative distributions of χ^2_M for M_F and for all four moments combined compared to the χ^2 cumulative distribution with $N = 1$ and 4 degrees of freedom. Tables 1 and 2 give the numerical values of the fits to $p(\chi_M)$ and the $\langle\chi^2_M\rangle$ values, respectively, for all 48 Balrog-injection tiles combined.

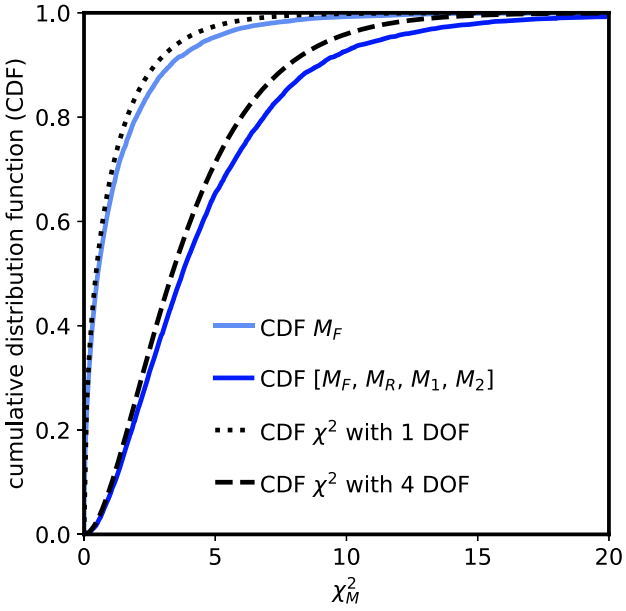

Figure 2. Cumulative distribution function (CDF) of χ^2_M for M_F (light blue) and $\boldsymbol{M} = [M_F, M_R, M_1, M_2]$ (dark blue) with $\langle\chi^2_M\rangle = 1.24$ and 4.64, respectively. For comparison, we plot the cumulative distribution functions of a χ^2 distribution with $N = 1$ (dotted black line) and 4 degrees of freedom (dashed black line). It is clear that the distribution of χ^2_M is not consistent with the hypothesis that the noise is purely due to shot noise from the sky background and detector read noise.

The widths of the distributions of χ_M are generically larger than $\sigma = 1.0$, which we observe across all DES Balrog-injection tiles and *griz* bands, indicating 6–30 per cent underestimates of the pixel variance. The width is largest for M_F, the flux moment, but is also significant in the second-order shape moments, particular M_R. In addition, we see that there is a small but significant sky oversubtraction of $\approx 0.13\sigma$, resulting in a negative μ offset in M_F, which is the only moment sensitive to a global sky offset because it is the only moment with non-zero weight on the $k = 0$ term of the Fourier space image, which equals the total flux of the real-space image.

The same trends are reflected in the χ^2_M test, where we see that the data are not consistent with χ^2 distribution of $N = 1$ or 4 degrees of freedom. This result suggests that there is additional noise contributing to our data which is not included in our measurement of the pixel noise due to the sky background and detector read noise.

Exploring further the sky oversubtraction, we show in Fig. 3 the μ offset from the noise test in each band as a function of object density per DES tile (object counts with $m_i < 23.5$) for the set of

Table 1. Mean (μ) and standard deviation (σ) values for noise test 1, with 'shot' denoting inclusion of background Poisson noise and read noise only, and 'shot+US' case including the measured US noise variance as well.

Moment	g		r		i		z	
	μ	σ	μ	σ	μ	σ	μ	σ
M_F								
Shot	0.019	1.127	−0.016	1.136	−0.022	1.113	−0.019	1.098
Shot+US	0.016	1.002	−0.015	1.026	−0.020	1.007	−0.018	1.013
M_R								
Shot	0.029	1.068	0.017	1.074	−0.000	1.068	−0.003	1.062
Shot+US	0.027	1.004	0.016	1.004	−0.000	0.998	−0.003	1.009
M_1								
Shot	0.001	1.052	0.003	1.058	−0.002	1.046	−0.003	1.040
Shot+US	0.001	1.019	0.003	1.026	−0.002	1.019	−0.003	1.019
M_2								
Shot	−0.004	1.041	−0.001	1.055	−0.001	1.047	−0.005	1.030
Shot+US	−0.004	1.011	−0.001	1.023	−0.001	1.022	−0.004	1.011

Notes. These results include a local sky subtraction as described in Section 3.1. The σ values are plotted in Fig. 6 as well.

Table 2. $\langle \chi^2_M \rangle$ from distributions shown in Fig. 7 for each band including shot noise only and shot+US noise, as described in Table 1.

moment	g $\langle \chi^2_M \rangle$	r $\langle \chi^2_M \rangle$	i $\langle \chi^2_M \rangle$	z $\langle \chi^2_M \rangle$
M_F				
shot	1.2714	1.2923	1.2406	1.2077
shot+US	1.0059	1.0548	1.0154	1.0272
$4M$				
shot	4.6574	4.7239	4.5891	4.5402
shot+US	4.1515	4.2351	4.1396	4.1811

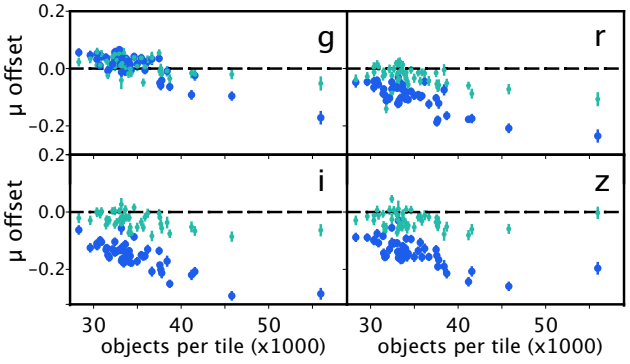

Figure 3. μ offset (as calculated in Fig. 1) as a function of object density per DES tile for 48 Balrog-injection tiles (blue). The four panels show data in *griz* bands. While the *g* band is relatively unaffected, we demonstrate that the sky has been oversubtracted in the *riz* bands, which tends to increase in areas of higher object density. The green dots show the μ offset after performing a local sky subtraction, which mitigates the flux bias.

48 Balrog-injection tiles. It is apparent that the *g* band is relatively unaffected, but moving to redder bands, we find larger offsets, which increase with object density. The mean μ offsets from all 48 Balrog-injection tiles are $\mu_g = 0.023$, $\mu_r = -0.08$, $\mu_i = -0.135$, and $\mu_z = -0.123$. We suspect that this oversubtraction may be due to (1) residual light from large, bright galaxies in the frame (similar to what was noted in Blanton et al. 2011), (2) scattered-light haloes from stars, and/or (3) errors in the SExtractor algorithm's treatment of the US component of background.

To mitigate this bias for BFD, we perform a local sky background subtraction by measuring the mean local background in a 2-pixel-wide frame around the postage stamp. We then convert this background into an offset in the flux moment M_F. We also compute the contribution to the variance in M_F by computing the uncertainty due to subtracting this local sky value from each pixel in the postage stamp. The background estimate should be computed after masking pixels that are allocated to detected sources by SExtractor. Because our tests are performed on isolated sources, this has minimal impact, but would need careful consideration in a more general approach that includes treatment of blended sources. The μ offset for each Balrog-injection tile after performing subtraction is shown in Fig. 3 (green), and the mean μ offsets from all 48 tiles are much closer to zero: $\mu_g = 0.019$, $\mu_r = -0.023$, $\mu_i = -0.022$, and $\mu_z = -0.025$. Removing the local background adds noise to the flux moment M_F, so we correct the shot/read noise variance for M_F by adding the variance from the sky measurement uncertainty. Thus, the local sky subtraction appears to reduce the mean sky error from 10–20 per cent of the sky noise for the SExtractor estimate to ≈ 2 per cent of sky noise, which is $\lesssim 1$ photoelectron. The nature of the residual biases are not yet understood.

The bias in sky estimation that we find is not just an issue for BFD flux moments; it will affect any flux measurement method, and many shape measurement methods. Indeed, a subsequent careful investigation of stellar fluxes across the DES survey has revealed flux-dependent systematic offsets that are characteristic of background subtraction errors, and also exhibits the same dependence of filter and field stellar density as we find (E. Rykoff, private communication). Investigation into the use of local sky estimates continues.

3.2 Empty sky cross power spectra

To assess the US noise contributing to our data, we use the 39 Balrog-variant tiles described in Section 2.2 to isolate postage stamps with empty sky. Within each tile, we find the postage stamps belonging to Balrog galaxies (that were not actually injected) and cut down the postage stamp to 32 × 32 pixels (the minimum postage stamp size for DES galaxies). Secondly, we require that no neighbors (detected, real galaxies) have SExtractor isophotes extending within the

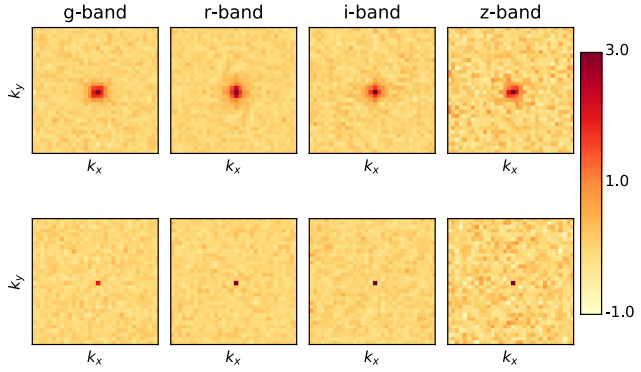

Figure 4. 2D average cross-power spectra of empty sky regions in *griz* bands for one DES Balrog-variant tile normalized to the 99th percentile power in each band (bottom panel is normalized to the same value as the top panel). Each panel has $k = 0$ at the centre, and the Nyquist frequency (0.5 cycles per pixel) at the borders. Top panel: Cross-power spectra are taken for all single-epoch images of one region; thus, sky background and detector noise should cancel, isolating any contribution from US. Bottom panel: Cross-power spectra are taken for single-epoch images of different regions; thus, sky background and detector noise, as well as US should cancel. Only background estimation errors, at $k = 0$, remain non-zero.

boundaries of the postage stamp, as indicated by the SExtractor segmentation maps.

For each postage stamp of empty sky, we measure the autopower spectra for each single-epoch image and the cross-power spectra of all combinations of the single-epoch images in the same filter. For $N > 1$ images, this gives $N!/2!(N-2)!$ possible combinations to produce cross-power spectra. Shot noise and read noise should average to zero in the cross-power spectra. If there are US below the detection threshold, they will contribute coherently to all single-epoch images and yield positive cross-power spectra.

To look for the US signal, we average the cross-power spectra over the entire Balrog-variant tile. The 2D average cross-power spectra for each band of one tile are shown in the top panel of Fig. 4. There is clearly a US signal present in all bands. To ensure that this is not an artefact of the instrument or detector, we also measure the cross-power spectra of distinct patches of blank sky (where the US signal as well as shot noise should average to zero). These 2D average cross-power spectra are shown in the bottom panel of Fig. 4, and it is evident that there is no signal in this case. The only significantly non-zero cross-power is the $k = 0$ (constant) term, which arises due to the systematic tendency to oversubtract the background.

The azimuthally averaged profiles of the cross-power spectra from empty regions of 39 Balrog-variant DES tiles are shown in Fig. 5, along with the average autopower spectra of the PSF of each tile. (The shading represents the standard deviation of profile shapes from the 39 different tiles.) The profiles are all normalized at $k = 0.5$, since the $k = 0$ term has extra noise due to sky background subtraction errors. We find that the averaged US population is resolved in all bands. To estimate the average size of US in each band, we convolve the PSF with Gaussians of varying σ and compare the resulting power spectrum with the average cross-power spectra of US (black dashed line). We find that $\sigma = 0.25$ arcsec for the *g*, *r*, and *i* bands and $\sigma = 0.32$ arcsec for the *z* band yield rough agreement with the US profile. Within the uncertainties of this measurement, the cross-power spectra are consistent with arising from a population of sources with a slightly resolved profile [intrinsic full width at half-maximum (FWHM) ≈ 0.7 arcsec, with the typical PSF of DES imaging having FWHM ≈ 0.9 arcsec in *riz* bands]. It is not entirely surprising that

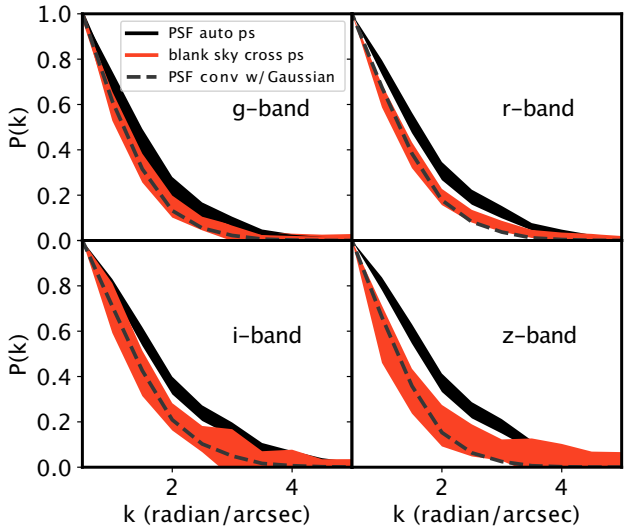

Figure 5. Profiles of cross-power spectra of empty patches for the *griz* bands averaged over 39 Balrog-variant tiles. The cross-power spectra are normalized to the power at $k = 0.05$. The orange shading shows the mean profile from all 39 tiles, with width representing the standard deviation. The black shading shows the mean profile of the average PSF autopower spectrum for each tile, with width representing the standard deviation. The grey dashed line shows the mean PSF profile convolved with a Gaussian of given σ, to estimate the rough size of the average US population. We find $\sigma \approx 0.25$, 0.25, 0.25, and 0.32 arcsec for *g*, *r*, *i*, and *z*, respectively.

the sizes should differ across bands, as the populations of US probed in each band will be slightly different.

3.3 Computing cross-covariance

We can treat the background source population as a roughly stationary noise source. While this should be strictly true for our randomly placed Balrog-injected galaxies, it will not be precisely true for real galaxies, for reasons we discuss in Section 4. We will proceed, however, to compute a new covariance matrix for the US noise which we will add to our nominal shot/read noise covariance matrix.

We could, in principle, use the cross-power spectrum computed in Section 3.2 to compute the US covariance of the moments, as described in equation (3) (see also equation 9 of Bernstein et al. 2016). However, this cross-power spectrum does not include corrections for the PSF and small pixel shifts for each individual image. These imperfections smear out the signal.

To compute the cross-covariance matrix more accurately, we compute the BFD moments for each image of empty sky. Using the BFD software enables us to properly account for the differing PSFs and world coordinate systems (i.e. registration) of each image. We then compute the empirical cross-covariance matrix of BFD moments, $\mathbf{Cov}_X$:

$$\mathbf{Cov}_{X[i,j]} = \frac{\sum_{\alpha,\beta,\alpha\neq\beta} M_{i\alpha} M_{j\beta}}{\sum_{\alpha,\beta,\alpha\neq\beta} 1}, \quad (6)$$

where (i, j) are indexes of the moment element of the covariance matrix, and α and β index are the exposures of this sky patch. The summation is performed over all combinations of images where $\alpha \neq \beta$. We combine data from all 39 Balrog-variant tiles to compute a global cross-covariance matrix for the DES data from empty sky regions.

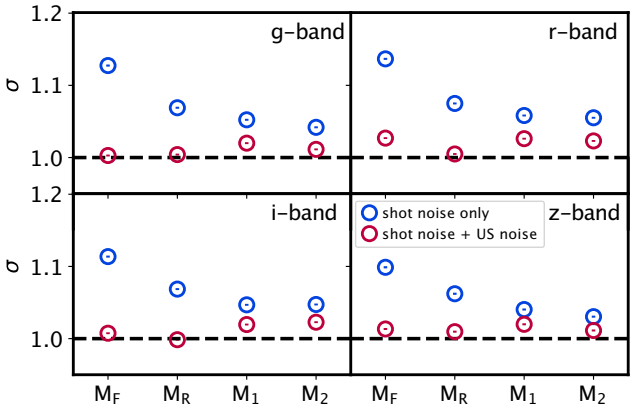

Figure 6. σ of χ_M distribution (blue) and χ_{MX} distribution (red) for each BFD moment from all 48 Balrog-injection tiles. Including the cross-covariance matrix brings the σ of the distribution closer to the expected value of 1. The values of σ for each band/moment combination are given in Table 1.

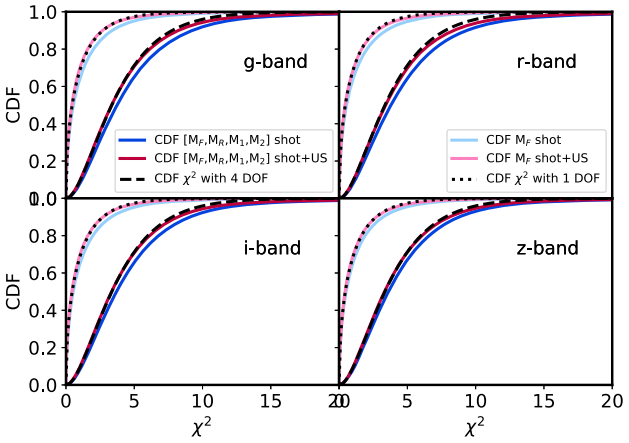

Figure 7. CDF of χ^2_M (blue/light blue) and χ^2_{MX} (red/pink) for the single BFD M_F moment and for the four M_F, M_R, M_1, and M_2 moments for each band over all 48 Balrog-injection tiles. The χ^2 CDFs with 1 (black dotted line) and 4 degrees of freedom (black dashed line) are plotted for reference. Again, we show that including the cross-covariance term brings the moment distribution closer to expectations. Mean χ^2 values for each distribution are given in Table 2.

Finally, we test how using the new cross-covariance matrix affects the noise tests described in Section 2.4. Analogous to χ_M, we now define χ_{MX}, which is now calculated using the sum of the shot/read-noise covariance and $\mathbf{Cov}_X$:

$$\chi_{MX} = \frac{M_D - M_T}{\sqrt{\sigma_M^2 + \sigma_X^2}}, \tag{7}$$

where σ_M is from the shot/read-noise covariance matrix and σ_X is from the cross-covariance matrix $\mathbf{Cov}_X$. Generalizing to the χ^2 test using arbitrary moments, we have

$$\chi^2_{MX} = (\boldsymbol{M}_D - \boldsymbol{M}_T)^T \left[\mathbf{Cov}_M + \mathbf{Cov}_X\right]^{-1} (\boldsymbol{M}_D - \boldsymbol{M}_T). \tag{8}$$

For these tests, we combine moments from all 48 Balrog-injection tiles, and compute the μ and σ of the normalized histogram (as in Fig. 1) for each band. We have subtracted the local sky estimate for each postage stamp and included the variance due to that local sky in the flux moment variance term of $\mathbf{Cov}_M$. In Fig. 6, we show the σ value for each band/moment combination using $\mathbf{Cov}_M$ and using $\mathbf{Cov}_M + \mathbf{Cov}_X$. We find general improvement using our globally defined cross-covariance term, with σ lowering from $\sim$1.12 to $\sim$1.01 for the flux moment, and dropping to similar levels for the other moments ($\sigma = 1.026$ in the worst case). We report the σ and μ values for all bands in Table 1.

Furthermore, in Fig. 7, we show the full χ^2 test for M_F only and for all four moments of a given band across all 48 Balrog tiles and we report the $\langle\chi^2_M\rangle$ value in Table 2. In all bands, we find that when including the cross-covariance matrix that characterizes the US noise, the CDF of the data more closely approaches the χ^2 distribution with the appropriate number of degrees of freedom. The $\langle\chi^2_M\rangle$ values also reflect the improvement, as they approach the expected value of 1 for M_F only and 4 when looking at the vector of four moments.

4 DISCUSSION

The above tests demonstrate that the measured distribution of moment errors is well described by a multivariate Gaussian distribution with covariance matrix $\mathbf{Cov}_M$ that sums the usual contribution from sky/read noise with an additional $\mathbf{Cov}_X$ term that is measured from inter-exposure correlations in 'blank' sky. A workable hypothesis is that $\mathbf{Cov}_X$ arises from the signals of undetected sources, i.e. the US noise. In this section, we examine the data further to infer the average properties of the US population under this hypothesis as well as discuss the validity of the assumption of stationarity made in this analysis.

4.1 Properties of background galaxies

In Section 3.2, we found that the US population is mildly resolved with typical sizes of $\sigma \sim 0.25$ arcsec for the g, r, and i bands, and 0.32 arcsec for the z band. Since each band probes different populations of background galaxies (as well as stars), it is not surprising that these values vary. Regardless, our US population consists largely of small galaxies that are slightly larger for redder bands.

As another check of our data, we can also compare the cross-power spectra computed in Section 3.2 with the predicted power spectra of US from the flux distribution of the DES data, noting that the power spectrum is defined by the flux distribution of sources in the image

$$P(k) = \int \mathrm{d}f \, \frac{\mathrm{d}n}{\mathrm{d}f} f^2 |s^2(k, f)|, \tag{9}$$

where $\mathrm{d}n/\mathrm{d}f$ is the flux f distribution of sources and $s(k, f)$ is their shape. Assuming that all US are the same small shape, when k is well below the size of the galaxies ($k \to 0$), we can define the power spectrum or variance of US:

$$V_{\rm US} = \int \mathrm{d}f \, \frac{\mathrm{d}n}{\mathrm{d}f} f^2. \tag{10}$$

Thus, to predict $V_{\rm US}$, we need to know the flux distribution of US in the data. To do this, we use equation (10) to measure the variance of sources with i-band magnitude >23.0 from both the wide field $V_{\rm wide}$ and the deep field $V_{\rm deep}$, which extends $\sim$1 mag deeper than the wide field. We then compute $V_{\rm US} = V_{\rm deep} - V_{\rm wide}$. In Fig. 8, we show the $k_y = 0$ slice of the mean cross-power spectra, normalized by the $V_{\rm US}$ in each band. Performing a Gaussian fit to the cross-power spectra (throwing out the central data points, which are contaminated by the sky background oversubtraction), we find that the normalized cross-power spectra are $\sim$1 at $k = 0$ (although for the z band, it is closer to 2). We expect that the ratio should be larger than 1, as we do not extrapolate the flux distribution to fainter magnitudes.

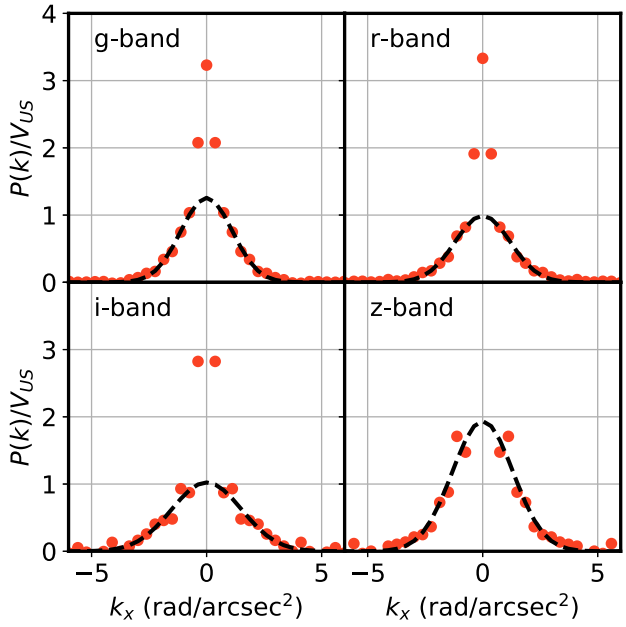

Figure 8. Cut along $k_y = 0$ slice of cross-power spectra (as shown in Fig. 4) normalized by $V_{\rm US}$ as described in Section 4.1 for all four bands. The black dashed line shows a Gaussian fit, ignoring the inner three values, which are contaminated by the noise from residual sky background subtraction issues. We find that the cross-power spectra from the data approaches the predicted value of $V_{\rm US}$, although for the z band, it is closer to $2 \times V_{\rm US}$.

4.2 Assumption of stationarity

In the analysis above, we have assumed that the noise due to US is stationary, i.e. the US galaxies are randomly sprinkled on the sky with respect to our detected population, and thus that the US noise covariance matrix $\mathbf{Cov}_X$ can be simply added to the shot-read noise covariance matrix $\mathbf{Cov}_M$. For the Balrog galaxies, which have been simply added to the DES tiles at a regular hexagonal grid of positions, this assumption is fully valid. However, we know that galaxies are clustered, and that US are clustered around brighter, detected galaxies, breaking our previous assumption. For example, Euclid Collaboration (2019) showed the clustering of galaxies of different magnitudes in the *HST* Ultra Deep Field (UDF), finding significant excess densities within ∼2 arcsec of objects with mag($F775W$) < 24.5, largely dominated by objects about 1 mag fainter than the chosen threshold.

Thus, we must consider two contributing sources to the US noise in our data: (1) pure projection US (at different redshifts) and (2) physically associated US at the same redshift. For projection US, we expect this signal to be stationary and fully captured by our Balrog simulations. There are some caveats that are not accounted for in Balrog, such as extinction by the foreground galaxy and magnification by the foreground galaxy or other matter along the line of sight. The first caveat would act to decrease the US signal. In nearby spiral galaxies, dust, as traced by the IR, generally follows the optical disc (Verstappen et al. 2013), although optical disc opacities are generally close to 0 by R_{25} (Holwerda et al. 2005). The second caveat might increase or decrease the US signal. Regardless, these are second-order effects on the primary US signal, which contributes ∼30 per cent extra variance. At our current 1 per cent level accuracy in noise determination, these are small effects.

For US that are physically associated with the detected galaxies (same redshift), there is an expected excess around the detected sources, breaking stationarity. Euclid Collaboration (2019) show that introducing clustered US galaxies produces a multiplicative bias $\sim 1 \times 10^{-2}$ for two shear estimation methods, whereas an unclustered US population induces a bias $\sim 4 \times 10^{-3}$ (with even the latter being larger than the required accuracy for imminent lensing surveys). The BFD method, however, relies on a template population built from deep sky images. If the template population includes clustered US at similar levels as in the wide-field population, BFD will naturally account for the signal due to clustered US in the Fourier moment space. Thus, the clustered US population will be treated as signal rather than noise, since it is subject to the same gravitational lensing distortion as the primary detected galaxy. In other words, we can consider the associated US photons to be part of the detected galaxy image. It will be important, however, to design the detection process such that (un)detected sources remain (un)detected after being subject to weak lensing distortions (Sheldon et al. 2019). Further simulations will be necessary to quantify the effectiveness of this strategy.

One other aspect of stationarity to consider is whether the derived US-noise matrix $\mathbf{Cov}_X$ is constant across the survey footprint in the face of varying survey noise levels and PSF size. Nominally, the answer is yes, since the BFD moments incorporate a PSF correction, and the shot noise itself is cancelled in the measurement of $\mathbf{Cov}_X$. It is true, however, that in regions of the survey with lower detection thresholds, there are fewer undetected sources so lower $\mathbf{Cov}_X$. Thus, there may need to be some adjustment of $\mathbf{Cov}_X$ for observing conditions unless we enforce a uniform detection threshold.

4.3 Metacalibration with undetected sources

The first-year weak-lensing analyses of the DES data make use of the 'metacalibration' technique (Huff & Mandelbaum 2017; Sheldon & Huff 2017), with implementation described by Zuntz et al. (2018). Forthcoming DES analyses will use the metadetection technique as well. Does the undetected source noise affect metacalibration? In this technique, a linear operator is applied to the observed image such that all objects in the scene undergo a (pre-seeing) shear operation. This will naturally apply the same shear to undetected sources as it does to the (targeted) detected sources, thus calibrating their effect correctly, albeit with the assumption that the US undergo identical shear to the target source. In practice, this is not true, for the same reasons that US noise is not stationary, but this is a second-order effect.

The image operator applied during metacalibration also shears the shot noise and read noise in the image. This is undesirable, since lensing does not shear the noise, and is compensated in the metacalibration algorithm by adding new noise to the image in a manner that re-symmetrizes the total noise (at a penalty in total noise amplitude). The US noise is not white noise and the re-symmetrization operation would not yield an unsheared realization of US noise; hence, it is better considered part of the sheared scene than the unsheared noise. We thus expect that the presence of US noise does not, to first order, alter the calibrations and results derived from metacalibration. The sky-level biases discussed herein will, however, have some impact on metacalibration and essentially any WL method that is sensitive to the sky level. Testing on simulations with undetected sources included indicates, so far, no detectable bias induced by their presence (Sheldon et al. 2019).

5 CONCLUSIONS

We have shown that US produce a significant noise contribution to DES images (up to 30 per cent in variance), which must be

characterized properly for accurate and precise determination of galaxy shapes for shear measurement. Treating the US noise as a stationary noise source, we can empirically compute a cross-covariance matrix for the BFD moments from empty sky regions in DES images. This cross-covariance matrix is then added to the shot/read noise covariance matrix to yield a covariance matrix that describes the observed BFD moment noise distribution to 1–5 per cent accuracy. Rather than requiring simulations to correct for this noise source, we have shown that BFD can treat the noise statistically, using these corrections derived directly from the sky images.

While we have explored and corrected these issues within the BFD shear-measurement scheme, the issues of sky misestimation and US noise will bias the mean and variance, respectively, of almost any measurements of flux and/or shape. Indeed, the effect of sky misestimation on stellar fluxes measured by SExtractor in the DES data releases has already been detected. BFD measurements are designed to have rigorously known uncertainties, which are amenable to correction for US noise. Other methods will need to consider how to treat US noise.

While the Balrog simulations do not fully capture the complexities of galaxy clustering versus pure projection, we suspect that our tests with this simplified population capture most of the problems. US clustered near faint galaxies should be present in both our target and template populations, and thus should be considered as part of the BFD signal, rather than noise. Magnification and dust obscuration are per cent level effects on top of the much larger effect described in this work. Future work may explore ways to improve the method shown here for surveys with more stringent requirements than DES.

ACKNOWLEDGEMENTS

We would like to thank Eric Neilsen and David Stark for helpful discussions on cross-correlating sky images and the dust extent in galaxies, respectively, and the anonymous referee for rapid and useful comments. KDE and GMB acknowledge support from NASA through a Research Support Agreement with grant 12-EUCLID11-0004, and grants AST-1615555 from the US National Science Foundation, and DE-SC0007901 from the US Department of Energy.

Funding for the DES Projects has been provided by the US Department of Energy, the U.S. National Science Foundation, the Ministry of Science and Education of Spain, the Science and Technology Facilities Council of the United Kingdom, the Higher Education Funding Council for England, the National Center for Supercomputing Applications at the University of Illinois at Urbana-Champaign, the Kavli Institute of Cosmological Physics at the University of Chicago, the Center for Cosmology and Astro-Particle Physics at the Ohio State University, the Mitchell Institute for Fundamental Physics and Astronomy at Texas A&M University, Financiadora de Estudos e Projetos, Fundação Carlos Chagas Filho de Amparo à Pesquisa do Estado do Rio de Janeiro, Conselho Nacional de Desenvolvimento Científico e Tecnológico and the Ministério da Ciência, Tecnologia e Inovação, the Deutsche Forschungsgemeinschaft and the Collaborating Institutions in the Dark Energy Survey.

The Collaborating Institutions are Argonne National Laboratory, the University of California at Santa Cruz, the University of Cambridge, Centro de Investigaciones Energéticas, Medioambientales y Tecnológicas-Madrid, the University of Chicago, University College London, the DES-Brazil Consortium, the University of Edinburgh, the Eidgenössische Technische Hochschule (ETH) Zürich, Fermi National Accelerator Laboratory, the University of Illinois at Urbana-Champaign, the Institut de Ciències de l'Espai (IEEC/CSIC), the Institut de Física d'Altes Energies, Lawrence Berkeley National Laboratory, the Ludwig-Maximilians Universität München and the associated Excellence Cluster Universe, the University of Michigan, the National Optical Astronomy Observatory, the University of Nottingham, the Ohio State University, the University of Pennsylvania, the University of Portsmouth, SLAC National Accelerator Laboratory, Stanford University, the University of Sussex, Texas A&M University, and the OzDES Membership Consortium.

This paper is based in part on observations at Cerro Tololo Inter-American Observatory, National Optical Astronomy Observatory, which is operated by the Association of Universities for Research in Astronomy (AURA) under a cooperative agreement with the National Science Foundation.

The DES data management system is supported by the National Science Foundation under Grant Numbers AST-1138766 and AST-1536171. The DES participants from Spanish institutions are partially supported by MINECO under grants AYA2015-71825, ESP2015-66861, FPA2015-68048, SEV-2016-0588, SEV-2016-0597, and MDM-2015-0509, some of which include ERDF funds from the European Union. IFAE is partially funded by the CERCA program of the Generalitat de Catalunya. Research leading to these results has received funding from the European Research Council under the European Union's Seventh Framework Program (FP7/2007-2013) including ERC grant agreements 240672, 291329, and 306478. We acknowledge support from the Brazilian Instituto Nacional de Ciência e Tecnologia (INCT) e-Universe (CNPq grant 465376/2014-2).

This paper has been authored by Fermi Research Alliance, LLC under Contract No. DE-AC02-07CH11359 with the US Department of Energy, Office of Science, Office of High Energy Physics.

DATA AVAILABILITY

The data underlying this paper will be shared on reasonable request to the corresponding author. This will be subject to the constraint that the Balrog images used herein are proprietary products of the Dark Energy Survey collaboration and not yet released for general public use.

REFERENCES

Bernstein G. M., Armstrong R., 2014, MNRAS, 438, 1880
Bernstein G. M., Armstrong R., Krawiec C., March M. C., 2016, MNRAS, 459, 4467
Bertin E., 2011, Astronomical Data Analysis Software and Systems XX, Automated Morphometry with SExtractor and PSFEx, Astronomical Society of the Pacific, San Francisco
Bertin E., Arnouts S., 1996, A&AS, 117, 393
Blanton M. R., Kazin E., Muna D., Weaver B. A., Price-Whelan A., 2011, AJ, 142, 31
Calvi V., Pizzella A., Stiavelli M., Morelli L., Corsini E. M., Dalla Bontà E., Bradley L., Koekemoer A. M., 2013, MNRAS, 432, 3474
Drlica-Wagner A. et al., 2018, ApJS, 235, 33
Euclid Collaboration et al., 2019, A&A, 627, A59
Hoekstra H., Viola M., Herbonnet R., 2017, MNRAS, 468, 3295
Holwerda B. W., Gonzalez R. A., Allen R. J., van der Kruit P. C., 2005, AJ, 129, 1396
Huff E., Mandelbaum R., 2017, preprint (arXiv:1702.02600)
Jarvis M. et al., 2016, MNRAS, 460, 2245
Kaiser N., Squires G., Broadhurst T., 1995, ApJ, 449, 460
Kashlinsky A., Arendt R. G., Mather J., Moseley S. H., 2005, Nature, 438, 45
Kashlinsky A., Arendt R. G., Ashby M. L. N., Fazio G. G., Mather J., Moseley S. H., 2012, ApJ, 753, 63
Morganson E. et al., 2018, PASP, 130, 074501
Rowe B. T. P. et al., 2015, Astron. Comput., 10, 121

Samuroff S. et al., 2018, MNRAS, 475, 4524
Sheldon E. S., Huff E. M., 2017, ApJ, 841, 24
Sheldon E. S., Becker M. R., MacCrann N., Jarvis M., 2019, preprint (arXiv: 1911.02505)
Suchyta E. et al., 2016, MNRAS, 457, 786
Tewes M., Kuntzer T., Nakajima R., Courbin F., Hildebrandt H., Schrabback T., 2019, A&A, 621, A36
Tonry J., Schneider D. P., 1988, AJ, 96, 807
Verstappen J. et al., 2013, A&A, 556, A54
Zuntz J., Kacprzak T., Voigt L., Hirsch M., Rowe B., Bridle S., 2013, MNRAS, 434, 1604
Zuntz J. et al., 2018, MNRAS, 481, 1149

APPENDIX A: BFD VALIDATION SIMULATIONS

Shear bias is typically quantified using a linear model $g_{\rm meas} = g_{\rm true}(1 + m) + c$. The validation simulations of Bernstein et al. (2016) showed a small but significant m bias ($m = 0.002$) that was unexpected, given the underlying design of BFD to be unbiased at small shear values. We have investigated the cause of the bias by re-performing these simulations, varying different properties to identify the cause of the bias.

For the base simulation, we use the GALSIM software package (Rowe et al. 2015) to draw galaxies on to postage stamps of size 48 x 48. Table A1 summarizes the basic properties of the simulations, which are similar to those in Bernstein et al. (2016). The pixel scale is 1 arcsec = 1 pixel, and henceforth any angular sizes will be in these units. Each galaxy is composed of a disc and bulge component, where the bulge fraction is drawn from a uniform distribution. The two components are drawn at slightly different offsets from the centre of the postage stamp. The half-light radius r_e is drawn from a uniform distribution of one to two times r_e of the PSF, which is drawn as a Moffat with $r_e = 1.5$ and $\beta = 3.5$. We additionally apply a small ellipticity $e_2 = 0.05$ to the PSF, to look for any additive bias from imperfect PSF correction. The galaxies are given unlensed ellipticity $e = (a^2 - b^2)/(a^2 + b^2)$ components e_1 and e_2 drawn from the distribution given in equation (A1) where $\sigma_e = 0.2$:

$$P(e) \propto (1 - e^2)^2 \exp \frac{-e^2}{2\sigma_e^2}. \quad \text{(A1)}$$

The background noise is kept at a constant level for each postage stamp. Galaxies are drawn with flux corresponding to a uniform distribution in S/N over the range of 5–25 for a standard circular galaxy. A constant shear is applied to all galaxies in a given simulation. We use the $k\sigma$ weight function defined in Bernstein et al. (2016) and given in equation (A2) with $N = 4$ and $\sigma = 3.5$:

$$W(|k^2|) = \begin{cases} \left(1 - \frac{k^2\sigma^2}{2N}\right)^N & k < \frac{\sqrt{2N}}{\sigma} \\ 0 & k \geq \frac{\sqrt{2N}}{\sigma} \end{cases}. \quad \text{(A2)}$$

To speed up tests, we no longer save images of galaxies to disc, now just saving the BFD moments directly to a table. Each simulation requires 1 billion galaxies to obtain an uncertainty on the multiplicative bias within the 10^{-3} multiplicative bias goal. The 1 billion galaxies are divided into batches of 500 000 targets and 10 000 templates. Each batch takes 10 CPU-hours, for a total of $\sim$ 20 000 CPU-hours for an entire simulation. We have used the NERSC computing resources to perform these simulations.

Table A1. Summary of simulation parameters.

Characteristic	Parameter
Galaxy profile	Bulge+disc (decentred)
Galaxy bulge fraction	$U(0,1)$
Galaxy r_e	$U(1.5–3)$ pixels
Galaxy S/N	$U(5–25)$
Galaxy e	$P(e)$ given by equation (A1)
Galaxy shape noise σ_e	0.2
PSF profile	Moffat ($\beta = 3.5$)
PSF size	$r_e = 1.5$ pixels
PSF ellipticity	$e_1 = 0.0$, $e_2 = 0.05$
Weight function	$k\sigma$ (equation A2)
Weight function N	4
Weight function σ	3.5
input shear $g_{1,\,\rm true}$	[0.02, 0.04, 0.06]
input shear $g_{2,\,\rm true}$	[0.0, 0.0, 0.0]
$N_{\rm batch}$ [target, template]	[5×10^5, 10^4]
$N_{\rm total}$	10^9

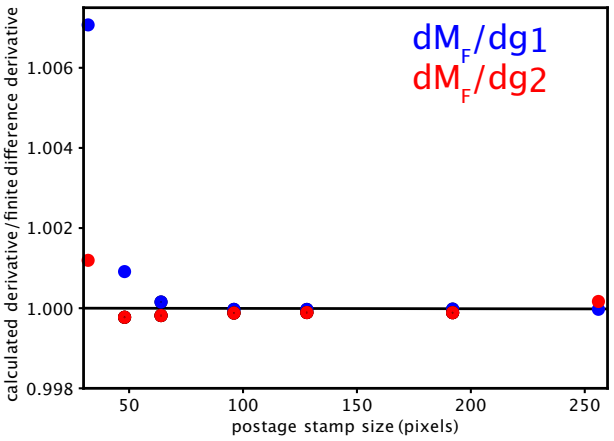

Figure A1. The flux moment derivative with respect to shear computed directly from the unsheared images using the formulas in Bernstein et al. (2016) divided by the same derivative computed using finite differences. The derivatives with respect to g_1 and g_2 are shown in blue and red, respectively. For smaller postage stamp sizes, the difference between the two is large compared to our target of $<10^{-3}$ errors. For our particular setup, a postage stamp size of 96 is sufficient to mitigate the issue. This pattern is seen with other moments and for higher order derivatives.

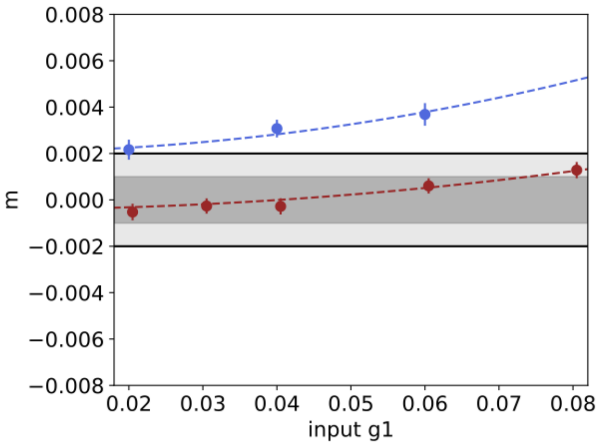

Figure A2. Multiplicative bias m versus input $g1$ shear. Blue points show data from Bernstein et al. (2016) simulations and red points show data from new simulations using images zero-padded to 96 × 96. A quadratic fit to the data yields $m = -0.0004$, well within the targets of next generation surveys (grey region).

We have investigated the source of this bias by altering the galaxy population in the simulations (e.g. using a single exponential profile) and by altering the image properties (e.g. the postage stamp size). We determined that the bias arises due to the numerical calculation of the moments and their derivatives. The moments are calculated by summing the Fourier space image of the galaxy's pixel image as given in equation (1). The derivatives are also computed as sums over Fourier space, as detailed in equations (C12) and (C13) of Bernstein et al. (2016). We use fast Fourier transforms to convert real-space images into Fourier space. The spacing in k-space is inversely related to the size of the postage stamp. By using a larger postage stamp size, we create a Fourier space image that is closer to the continuous function to be integrated.

We find that the size of the postage stamp is critical for obtaining the correct value of the moments and their derivatives, especially for the $\partial M_F/\partial g_1$. We compared the derivatives under shear inferred from the unsheared postage stamps to those computed using finite differences between sheared postage stamps. Fig. A1 shows that increasing the postage stamp size results in more precise agreement with the finite-difference estimate.

In real applications, we do not wish to use a large postage stamp, since that increases the interference from neighboring galaxies. Thus, in our simulations, we zero-pad the postage stamps from size 48×48 to 96×96 before Fourier transforming. In Fig. A2, we show the simulation results from Bernstein et al. (2016) (blue) and from our new zero-padded validation simulations (red). We find that $m = -0.00052 \pm 0.00035$ for input $g = 0.02$ after zero-padding the images, compared to $m = 0.002 \pm 0.0004$ found in the Bernstein et al. (2016) simulations. The zero-padding thus yields consistency with $m = 0$ and the desired level.

[1]*Department of Physics and Astronomy, University of Pennsylvania, Philadelphia, PA 19104, USA*
[2]*Department of Physics, ETH Zurich, Wolfgang-Pauli-Strasse 16, CH-8093 Zurich, Switzerland*
[3]*Kavli Institute for Particle Astrophysics & Cosmology, PO Box 2450, Stanford University, Stanford, CA 94305, USA*
[4]*Center for Cosmology and Astro-Particle Physics, The Ohio State University, Columbus, OH 43210, USA*
[5]*Santa Cruz Institute for Particle Physics, Santa Cruz, CA 95064, USA*
[6]*Department of Physics, Stanford University, 382 Via Pueblo Mall, Stanford, CA 94305, USA*
[7]*SLAC National Accelerator Laboratory, Menlo Park, CA 94025, USA*
[8]*Department of Astronomy, University of Illinois at Urbana-Champaign, 1002 W. Green Street, Urbana, IL 61801, USA*
[9]*National Center for Supercomputing Applications, 1205 West Clark St, Urbana, IL 61801, USA*
[10]*Jet Propulsion Laboratory, California Institute of Technology, 4800 Oak Grove Dr., Pasadena, CA 91109, USA*
[11]*Fermi National Accelerator Laboratory, PO Box 500, Batavia, IL 60510, USA*
[12]*Brookhaven National Laboratory, Bldg 510, Upton, NY 11973, USA*
[13]*Cerro Tololo Inter-American Observatory, National Optical Astronomy Observatory, Casilla 603, La Serena, Chile*
[14]*Departamento de Física Matemática, Instituto de Física, Universidade de São Paulo, CP 66318, São Paulo, SP 05314-970, Brazil*
[15]*Laboratório Interinstitucional de e-Astronomia – LIneA, Rua Gal. José Cristino 77, Rio de Janeiro, RJ-20921-400, Brazil*
[16]*Instituto de Fisica Teorica UAM/CSIC, Universidad Autonoma de Madrid, E-28049 Madrid, Spain*
[17]*LSST, 933 North Cherry Avenue, Tucson, AZ 85721, USA*
[18]*Physics Department, University of Wisconsin-Madison, 2320 Chamberlin Hall, 1150 University Avenue, Madison, WI 53706-1390, USA*
[19]*Department of Physics and Astronomy, University College London, Gower Street, London WC1E 6BT, UK*
[20]*Instituto de Astrofisica de Canarias (IAC), E-38205 La Laguna, Tenerife, Spain*
[21]*Departamento de Astrofísica, Universidad de La Laguna, E-38206 La Laguna, Tenerife, Spain*
[22]*Institut de Física d'Altes Energies (IFAE), The Barcelona Institute of Science and Technology, Campus UAB, E-08193 Bellaterra (Barcelona), Spain*
[23]*INAF-Osservatorio Astronomico di Trieste, via G. B. Tiepolo 11, I-34143 Trieste, Italy*
[24]*Institute for Fundamental Physics of the Universe, Via Beirut 2, I-34014 Trieste, Italy*
[25]*Observatório Nacional, Rua Gal. José Cristino 77, Rio de Janeiro, RJ-20921-400, Brazil*
[26]*Centro de Investigaciones Energéticas, Medioambientales y Tecnológicas (CIEMAT), E-28040 Madrid, Spain*
[27]*Department of Physics, IIT Hyderabad, Kandi, Telangana 502285, India*
[28]*Faculty of Physics, Ludwig-Maximilians-Universität, Scheinerstr. 1, D-81679 Munich, Germany*
[29]*Department of Astronomy/Steward Observatory, University of Arizona, 933 North Cherry Avenue, Tucson, AZ 85721-0065, USA*
[30]*Department of Astronomy, University of Michigan, Ann Arbor, MI 48109, USA*
[31]*Department of Physics, University of Michigan, Ann Arbor, MI 48109, USA*
[32]*Kavli Institute for Cosmological Physics, University of Chicago, Chicago, IL 60637, USA*
[33]*Institut d'Estudis Espacials de Catalunya (IEEC), E-08034 Barcelona, Spain*
[34]*Institute of Space Sciences (ICE, CSIC), Campus UAB, Carrer de Can Magrans, s/n, E-08193 Barcelona, Spain*
[35]*Département de Physique Théorique and Center for Astroparticle Physics, Université de Genève, 24 quai Ansermet, CH-1211, UK*
[36]*Department of Physics, The Ohio State University, Columbus, OH 43210, USA*
[37]*Center for Astrophysics|Harvard and Smithsonian, 60 Garden Street, Cambridge, MA 02138, USA*
[38]*Australian Astronomical Optics, Macquarie University, North Ryde, NSW 2113, Australia*
[39]*Lowell Observatory, 1400 Mars Hill Rd, Flagstaff, AZ 86001, USA*
[40]*George P. and Cynthia Woods Mitchell Institute for Fundamental Physics and Astronomy, and Department of Physics and Astronomy, Texas A&M University, College Station, TX 77843, USA*
[41]*Department of Astrophysical Sciences, Princeton University, Peyton Hall, Princeton, NJ 08544, USA*
[42]*Institució Catalana de Recerca i Estudis Avançats, E-08010 Barcelona, Spain*
[43]*Institute of Astronomy, University of Cambridge, Madingley Road, Cambridge CB3 0HA, UK*
[44]*Department of Physics and Astronomy, University of Sussex, Pevensey Building, Brighton BN1 9QH, UK*
[45]*School of Physics and Astronomy, University of Southampton, Southampton SO17 1BJ, UK*
[46]*Physics Department, Brandeis University, 415 South Street, Waltham, MA 02453, USA*
[47]*Computer Science and Mathematics Division, Oak Ridge National Laboratory, Oak Ridge, TN 37831, USA*
[48]*Institute of Cosmology and Gravitation, University of Portsmouth, Portsmouth PO1 3FX, UK*
[49]*Institute of Astronomy, University of Cambridge, Madingley Road, Cambridge CB3 0HA, UK*
[50]*Fakultät für Physik, Ludwig-Maximilians Universität München, Universitäts-Sternwarte, Scheinerstr. 1, D-81679 München, Germany*
[51]*Institute for Astronomy, University of Edinburgh, Edinburgh EH9 3HJ, UK*

This paper has been typeset from a TEX/LATEX file prepared by the author.